CHAPTER XI

PROBING SURFACE DEFECT (Ti^{3+}) ON TiO_2 NANOCRYSTAL WITH $H_3Re_3(CO)_{12}$

Since the discovery of photocatalytic water splitting by titania electrodes [131], the surface chemistry of titania has been investigated extensively, often with the goals of improved properties for photocatalytic reactions [147], sensor applications, and applications as a support for catalytic groups [148]. Numerous investigations of titania surfaces have been carried out with single crystals under ultrahigh vacuum conditions, typically with samples lacking hydroxyl groups; some investigations have focused on the defect sites [14]. Henrich and Kurtz [13] showed that the dominant defect sites on the rutile (110) surface are oxygen vacancies (Ti^{3+} sites). Yamazaki et al. [2] and Park et al. [3], reported that an increase of the density of these surface defects can enhance the photoactivity by photoelectron trapping. Surface defects have also been inferred to play a significant role enhancing the dispersion of metals on high-area porous TiO_2 [148].

Surface defects can be created by treatment of rutile (110) (or anatase) under vacuum [37,39,149] or in H_2 [150], or by ion bombardment [35] or exposure to electron beams [151]. Electron-beam exposure can produce exclusively Ti^{3+} sites and less severe surface damage than results from ion bombardment [151],[Error! Reference source not found.] which gives a variety of defects Ti^{n+} (n = 0–3) and can produce high densities of defects. Vacuum treatment can also produce almost exclusively Ti^{3+} sites, which may be structurally more uniform than those produced by the other methods [152]. The vacuum treatment also does less structural damage to the titania surface than H_2 treatment or ion bombardment [153].

Titania surfaces incorporating Ti^{3+} sites can be monitored with techniques including X-ray photoelectron spectroscopy [154], ultraviolet photoelectron spectroscopy [18], and electron paramagnetic resonance (EPR) spectroscopy [16]. Molecular probes

have also been used to characterize defect sites on rutile (110) by thermal desorption (temperature-programmed desorption), with the probe molecules being O_2 (which is photodesorbed[Error! Reference source not found.]) and CO_2 and CO, which are thermally desorbed [39,50]. These methods distinguish Ti^{3+} from Ti^{4+} sites, for example.

The probe molecules O_2, CO, and CO_2 that have been used to characterize rutile (110) are weakly bound to the defect sites, being desorbed at temperatures well below ambient. And although anatase is known to be more reactive and have higher surface areas than rutile for several photocatalytic applications [147], there are still no reports of investigations of anatase surface defects with probe molecules. Our goal was to characterize the surface sites of anatase (prepared in a high-area porous form with surface hydroxyl groups) by a probe molecule of another class, one that would be rather strongly bound and offer spectroscopic signatures to help elucidate its interactions with the surface.

Thus, we chose a metal carbonyl with a relatively high molecular weight, $H_3Re_3(CO)_{12}$, because it offers the following potential advantages, which we have assessed in the research described here:

- the ν_{CO} spectra are sensitive indicators of the bonding of $H_3Re_3(CO)_{12}$ to the surface;
- because $H_3Re_3(CO)_{12}$ is a proton donor, its reactions can provide evidence of the basic character of the surface sites on which it adsorbs;
- extended X-ray absorption fine structure (EXAFS) spectra can be used to determine the bond distances in the adsorbed probe molecule, giving evidence of its interaction with the surface.

Complementing the characterization methods listed in this paragraph, we also used infrared (IR) spectroscopy to characterize the surface OH groups and EPR spectroscopy to determine the numbers of radicals and defect sites (Ti^{3+}) on the titania surface.

Table 11.1: Sample characteristics and notation

Sample name	Treatment
TiO_2	none
TiO_{2ox}	O_2 at 723 K for 4 h
TiO_{2vac}	vacuum at 723 K for 4 h

11.1 XRD Data Characterizing Titania before and after Treatment

XRD was used to characterize the (untreated) TiO_2 sample and the treated samples TiO_{2ox}, and TiO_{2vac}. The XRD pattern of each sample (Figures 11.1A–C) includes strong, sharp peaks at 25°, 38°, 48°, 54°, 55°, 63°, 69°, 70°, and 75°, matching that of anatase (JCPDS No. 21-1272) [155]. The relative intensities of the various XRD peaks increased slightly as a result of the treatments, and each treatment gave essentially the same XRD pattern. Thus, we infer that (a) the small observed changes depend on the time of the treatment and not the atmosphere, (b) the bulk anatase structure was maintained in both treatments [70], and (c) any significant changes resulting from the treatments were in the surface structure of the titania rather than the bulk.

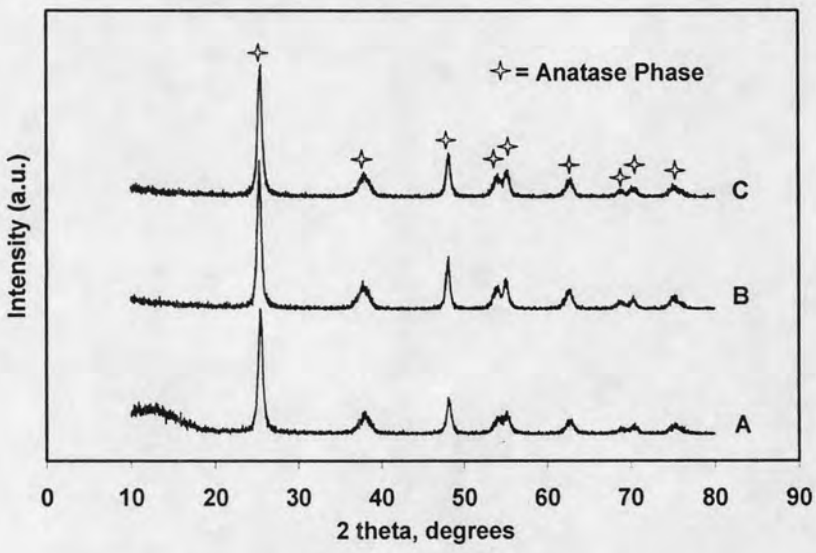

Figure 11.1:XRD patterns of titania samples: (A) TiO_2, (B) TiO_{2ox}, and (C) TiO_{2vac}.

11.2 EPR Evidence of Radical Species on Titania before and after Treatment

The EPR spectra of TiO_2, TiO_{2ox}, and TiO_{2vac} are shown in Figure 11.2. The spectrum of TiO_2 (Figure 11.2A) is in agreement with literature data [16,64,80,81,156] and essentially matches that of TiO_{2ox} (Figure 2B). These spectra include signals in three groups, designated A, B, and C, which are considered separately below and summarized in Table 11.2: A, $g_1 = 2.025$, $g_2 = 2.009$, $g_3 = 2.004$; B, $g_1 = 2.013$, $g_2 = 2.007$; and C, $g_1 = 1.989$, $g_2 = 1.935$.

In contrast, the signals in the spectrum of the evacuated sample TiO_{2vac} are more intense (Figure 11.2C), as expected [39,152,157]. The strong features are classified into the same groups mentioned above (Table 11.2): A, $g_1 = 2.025$, $g_2 = 2.009$, $g_3 = 2.004$ (however, the signal at $g_2 = 2.009$ is not resolved, because it was saturated; and C, $g_1 = 1.989$, $g_2 = 1.935$. A measurement was also made with a lower amplitude and sweep width (Figure 11.2D), allowing deconvolution of the $g_2 = 2.009$ peak into peaks at 2.011, 2.009, and 2.007 (Table 11.2); these resolved signals are similar to those observed in the spectrum of TiO_2 prior to the vacuum treatment (Figure 11.2A).

The EPR results agree well with literature reports, as summarized in Table 11.2; details follow: Thus, the signals in group C observed for all three samples ($g_1 = 1.989$, $g_2 = 1.935$) match within error those characterizing commercially available TiO_2 (P-25, Degussa, which consists of approximately 75% anatase and 25% rutile) [158] after H_2 treatment at 773 K [159]. These signals have been ascribed to Ti^{3+} surface defect sites formed by removal of lattice oxygen [159]. They are also close to the signals attributed to Ti^{3+} sites that were observed for anatase treated under vacuum or in O_2 and characterized by EPR spectroscopy during UV irradiation [16,80].

The signals of group A characterizing the three samples (g_1 = 2.025, g_2 = 2.009, g_3 = 2.004) agree well with those found to represent O_2^- species on the anatase surface (Table 11.2) [64,80]. The signals in group B characterizing all three samples (g_1 = 2.013, g_2 = 2.007) are very close to those found to represent O^- species on titania surfaces (Table 11.2) [64,165].

In summary, the EPR results agree well with the literature and show strong increases in the number of Ti^{3+} surface defects as well as O_2^- and O^- species as a result of the treatment under vacuum at 723 K [156,157].

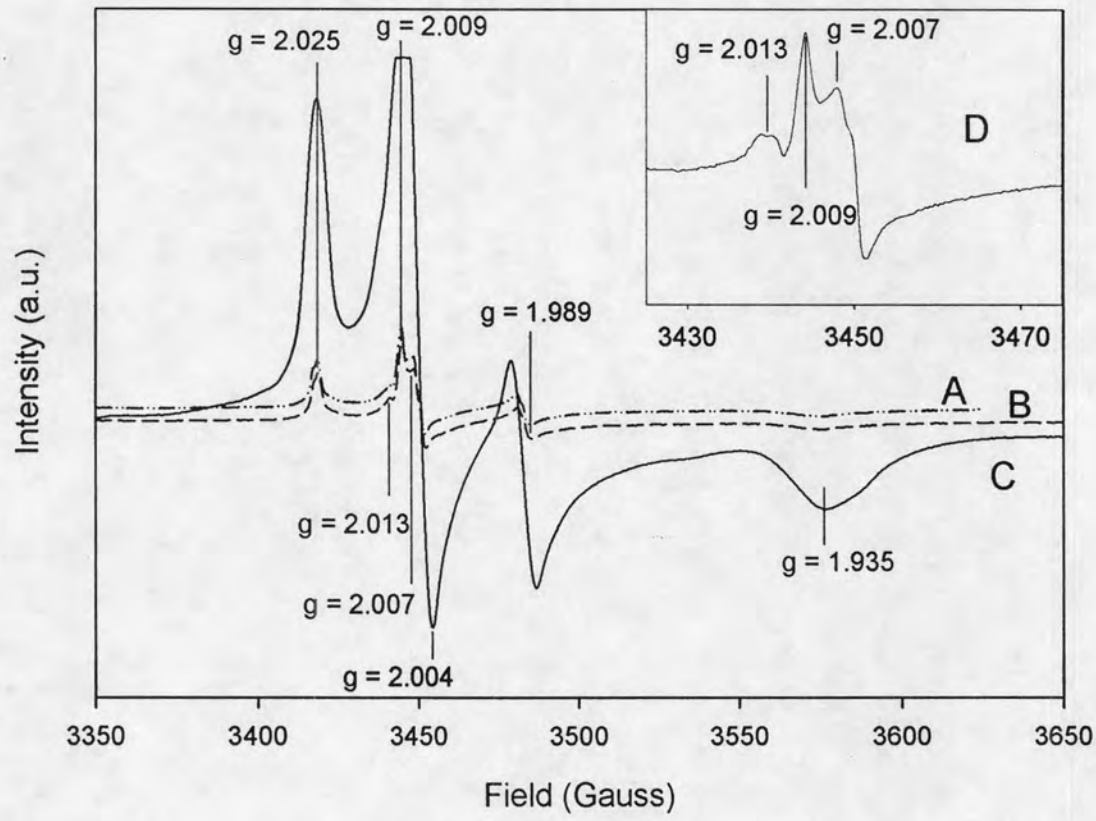

Figure 11.2: EPR spectra of titania samples: (A) TiO_2 (offset for clarity), (B) TiO_{2ox}, (C) TiO_{2vac}, and (D) TiO_{2vac} and using a lower amplitude and sweep width than in (C).

Table 11.2: Results of EPR Spectroscopy and Comparison with Literature: g Values characterizing Radicals formed on Anatase Surface

Sample	Treatment	Environment during EPR measurement	Radical/species	*g* value			Ref.
				g_1	g_2	g_3	
anatase	vacuum, 298 K	UV irradiation	Ti^{3+} (surface)	1.990		1.960	
anatase	O_2, 973 K	UV irradiation	Ti^{3+} (surface)	1.990		1.957	
Degussa P-25[a]	H_2, 773 K	-	Ti^{3+} (surface)	1.980		1.930	
anatase	O_2, 723 K	vacuum	Ti^{3+} (surface)	1.989		1.935	This work
anatase	vacuum, 723 K	vacuum	Ti^{3+} (surface)	1.989		1.935	This work
anatase	hydration	vacuum	O_2^- (surface, not form from O_2)	2.025	2.009	2.003	
anatase	-	O_2	O_2^- (surface)	2.024	2.009	2.003	
anatase	O_2, 723 K	vacuum	O_2^- (surface)	2.025	2.009	2.004	This work
anatase	vacuum, 723 K	vacuum	O_2^- (surface)	2.025	2.009	2.004	This work
anatase	hydration	UV irradiation	O^- (surface)	2.016	2.012	2.002	
TiO_2 colloid	-	water	O^- (surface)	2.014	2.007		
anatase	O_2, 723 K	vacuum	O^- (surface)	2.013	2.007		This work
anatase	vacuum, 723 K	vacuum	O^- (surface)	2.013	2.007		This work

11.3 OH groups on Titania before and after Treatment

The IR spectra of TiO_2, TiO_{2ox}, and TiO_{2vac} are shown in Figure 11.3. The spectrum of TiO_2 essentially matches that of TiO_{2ox} (Figures 11.3A and B), including two strong peaks, at 3673 and 3716 cm^{-1}, and two shoulders, at 3640 and 3687 cm^{-1}. On the basis of the literature results summarized in Table 11.3, the peaks at 3673 and 3716 cm^{-1} are assigned to OH groups bonded to Ti^{4+} and to Ti^{3+}, respectively [108,109,110]. The shoulder at 3640 cm^{-1} is attributed to a bridging OH group $(Ti^{4+})_2$-OH [108,109]. The shoulder at 3687 cm^{-1} has been assigned to OH groups terminally bonded to Ti^{4+},**Error! Reference source not found.** but we regard this assignment as less than firmly established.

The IR spectrum of TiO_{2vac} (Figure 11.3C) includes two strong peaks, at 3671 and 3716 cm^{-1}. A comparison with the spectrum of Figures 11.3A and B shows that the treatment under vacuum led to a strong increase in intensity of the band at 3716 cm^{-1} relative to that at approximately 3671 cm^{-1}, indicating a strong increase in the number of Ti^{3+}–OH groups relative to Ti^{4+}–OH groups. This treatment also led to the removal of bridging OH groups, indicated by the strong decrease in intensity of the peak at 3640 cm^{-1} (Figure 11.3C) as well as a strong increase in intensity of the EPR signals characterizing Ti^{3+} surface defect sites (Figure 11.2).

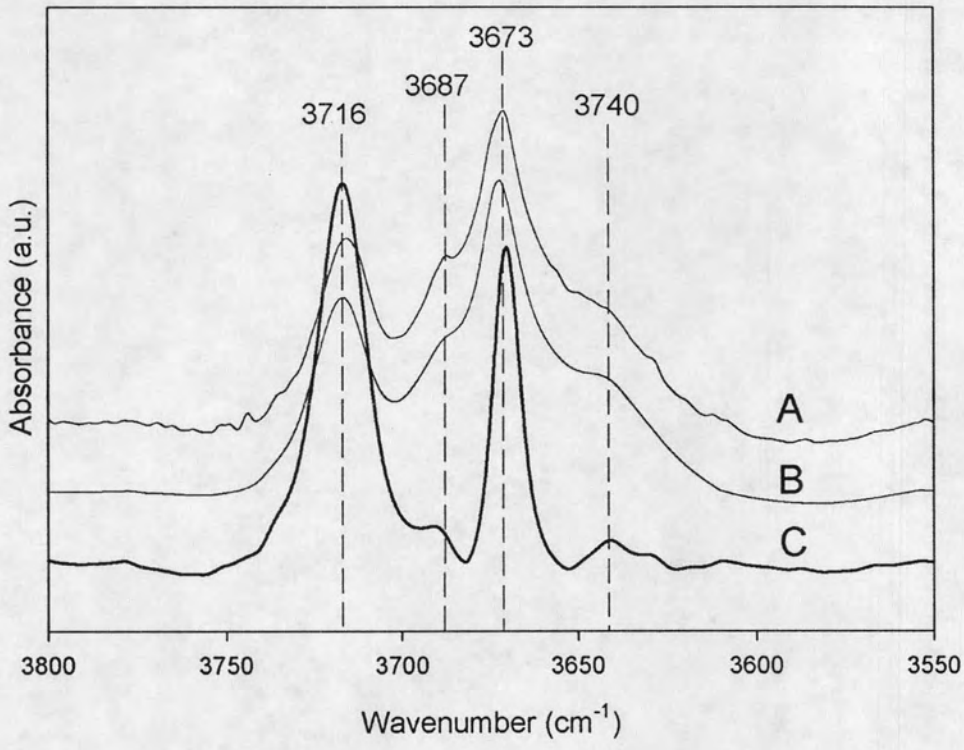

Figure 11.3: Normalized IR spectra in the ν_{OH} region characterizing titania samples: (A) TiO_2 (B) TiO_{2ox}, and (C) TiO_{2vac}. Normalization was done by matching the heights of the peaks at approximately 3673 cm^{-1}

Table 11.3: Infrared Bands in the OH Stretching Region Characterizing TiO_2

Sample	Sample treatment	Environment during IR measurement	ν_{OH} (cm^{-1})	Species	Ref.
Degussa P-25[a]	UV irradiation	vacuum	3716	Ti^{3+}–OH^-	1
Degussa P-25[a]	Partial deuteration	O_2	3716	Ti^{3+}–OH^-	1
anatase	O_2, 723 K	vacuum	3716	Ti^{3+}–OH^-	This work
anatase	vacuum, 723 K	vacuum	3716	Ti^{3+}–OH^-	This work
Degussa P-25	UV irradiation	vacuum	approximately 3670	Ti^{4+}–OH	1
Degussa P-25	Partial deuteration	O_2	approximately 3670	Ti^{4+}–OH	1
anatase	NH_3, 373–873 K	-	3685–3700	Ti^{4+}–OH	3
anatase	-	-	3670	Ti^{4+}–OH	4
anatase	O_2, 723 K	vacuum	3687, 3673	Ti^{4+}–OH	This work
anatase	vacuum, 723 K	vacuum	3687, 3671	Ti^{4+}–OH	This work
anatase	-	-	3640	$(Ti^{4+})_2$–OH	4
Degussa P-25[a]	-	pyridine	3640	$(Ti^{4+})_2$–OH	5
anatase	O_2, 723 K	vacuum	3640	$(Ti^{4+})_2$–OH	This work
anatase	vacuum, 723 K	vacuum	3640	$(Ti^{4+})_2$–OH	This work

[a] Mixture of anatase (75 %) and rutile (25 %)

11.4 Rhenium Carbonyls formed from $H_3Re_3(CO)_{12}$ on Treated Titania

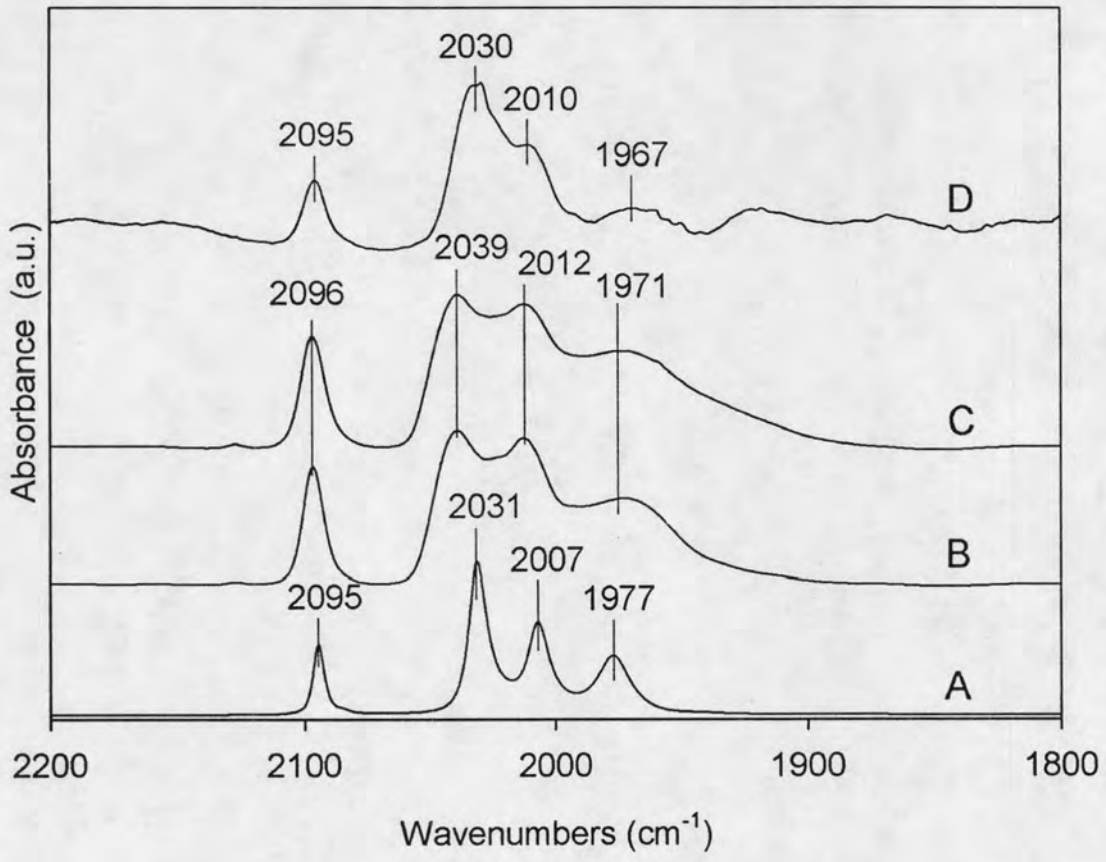

Figure 11.4: Normalized IR spectra in the ν_{CO} region characterizing: (A) $H_3Re_3(CO)_{12}$ in CH_2Cl_2 solution, (B) 1.0 wt% Re on TiO_{2ox} formed from $H_3Re_3(CO)_{12}$; (C) 1.0 wt% Re on TiO_{2vac} formed from $H_3Re_3(CO)_{12}$; and (D) 0.1 wt% Re on TiO_{2vac} formed from $H_3Re_3(CO)_{12}$. Normalization was done by matching the height of the peak at approximately 2031 cm^{-1}.

The IR spectra characterizing the ν_{CO} region of (a) $H_3Re_3(CO)_{12}$ in CH_2Cl_2 solution, samples formed from $H_3Re_3(CO)_{12}$ containing (b) 1 wt% Re on TiO_{2ox} and (c) 1 wt% Re on TiO_{2vac}, and containing (d) 0.1 wt% Re on TiO_{2vac} are shown in Figures 4A, B, C, and D, respectively. The ν_{CO} IR spectrum characterizing $H_3Re_3(CO)_{12}$ in CH_2Cl_2

solution (Figure 4A) includes strong peaks at 2094, 2032, 2008, and 1977 cm^{-1}, representing carbonyl groups bonded to the triangular rhenium frame [160,161]. The spectra characterizing the species formed from $H_3Re_3(CO)_{12}$ on TiO_{2ox} and TiO_{2vac} are similar, but with broadened and shifted ν_{CO} peaks, consistent with the results of Kirlin et al.[Error! Reference source not found.] [161] for species formed from $H_3Re_3(CO)_{12}$ adsorbed on γ-Al_2O_3 and on MgO. The peak broadening is attributed to the intrinsic nonuniformity of the surfaces and the consequent variations in adsorbate structure [162]. A summary of the IR absorption bands of rhenium carbonyls on various supports is given in Table 3.

The ν_{CO} IR spectra characterizing the TiO_{2vac} samples incorporating $H_3Re_3(CO)_{12}$ with 1.0 and 0.1 wt% Re loadings (Figures 4C and D) show the same IR features. The shifts appear to be different, but there is no pattern established by the data, and the differences may be insignificant within error.

Table 11.4: CO Stretching Frequencies of Adsorbed Rhenium Carbonyls Formed from $H_3Re_3(CO)_{12}$ and various supports

Loading of Re in sample, wt%	Surface/treatment	□CO bands (cm^{-1})	Ref.
1.0	TiO_2 treated with O_2 at 723 K	2096 (s), 2039 (m), 2012 (m), 1971 (mw)	this work
1.0	TiO_2 treated with vacuum at 723 K	2096 (s), 2039 (m), 2012 (m), 1970 (mw)	this work
0.1	TiO_2 treated under vacuum at 723 K	2095 (s), 2030 (m), 2010 (m), 1967 (mw)	this work
1.3	γ-Al_2O_3	2098 (m), 2032 (b), 2013 (b), 1966 (sh)	
2.2	MgO	2096 (s), 2000 (s), 1978 (s), 1872(s)	

The ν_{CO} bands for $H_3Re_3(CO)_{12}$ in a dichloromethane solution, are 2095(s), 2031 (s), 2007 (s), and 1977 (sm), which agree well those reported in the literature, Namely, 2096 (s), 2035 (s), 2012 (s), and 1979 (s).

11.5 OH Groups on Treated Titania with Adsorbed Rhenium Carbonyls.

There was no influence of remnants of the *n*-pentane used in the sample preparation on the IR spectra characterizing either of the treated titania samples, TiO_{2ox} and TiO_{2vac} (SI 1), but adsorption of rhenium carbonyls led to changes in the IR spectra of the titania.

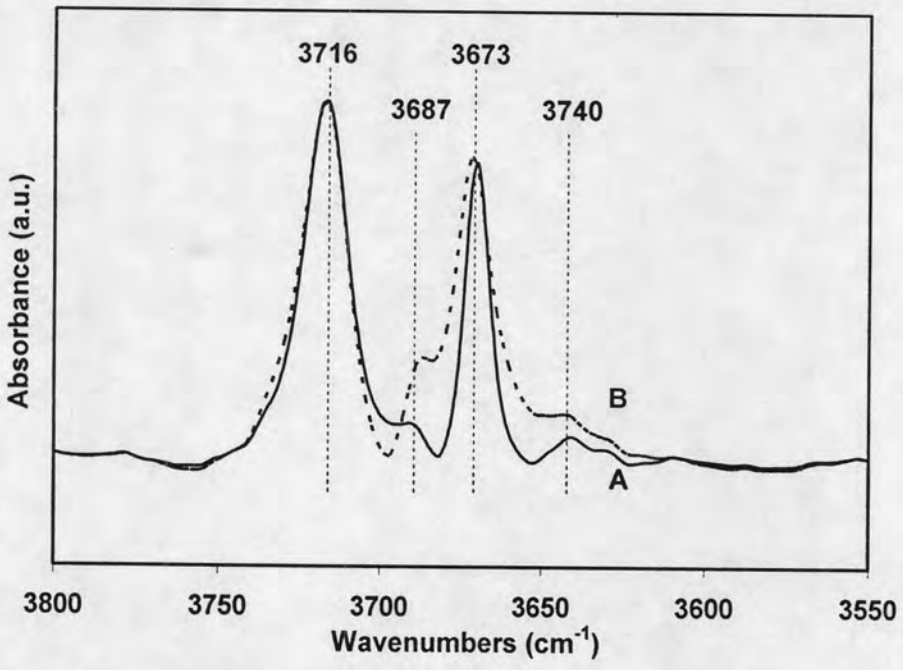

SI 1: IR spectra of (A) $TiO_{2\ vac}$ and (B) blank $TiO_{2\ vac}$ (titania + pentane)

The ν_{OH} IR spectrum characterizing the TiO_{2ox} incorporating adsorbed rhenium carbonyls with a 1.0 wt% Re loading (Figure 11.5A) shows the same features as the sample with clusters adsorbed on TiO_{2vac} at the same loading (Figure 11.5B). Adsorption of $H_3Re_3(CO)_{12}$ caused the peak at 3716 cm^{-1} to decrease strongly in intensity relative to that at 3673 cm^{-1}, accompanied by an increase in intensity of the shoulder at 3640 cm^{-1}. These results indicate that adsorption of $H_3Re_3(CO)_{12}$ led to the conversion of terminally bonded OH groups at Ti^{3+} sites and the formation of bridging OH groups.

When $H_3Re_3(CO)_{12}$ was adsorbed on TiO2vac at a loading of 1.0 wt% Re, a new IR peak was observed at 3610 cm-1 (Figure 5). Adsorption of H3Re3(CO)12 on TiO2vac led to a band at 3610 cm^{-1}. The position of this band matches to that of gas-phase H2O2. Connor et al. [163] assigned the nearby band at 3600 cm^{-1} to OH groups weakly bonded to titania; thus, the assignment of this band is still debated. These observations are consistent with those of Szczepankiewiez et al., [108] who observed a band at 3610 cm-1 characterizing a titania sample that had been treated under vacuum at high temperature and then exposed to HCl; however, they did not assign the band. The observed decrease in the number of O_2- species and the appearance of the band at 3610 cm-1 might be explained as a result of another reaction with $H_3Re_3(CO)_{12}$, as follows: The proton could interact with O_2- to form HO_2, which could be converted into other products [164]. Nakamura et al. [165] reported that O_2^- in acidic solutions reacted to give such an intermediate and then to H_2O_2

To test the inference that the decrease in the number of OH groups bonded to Ti^{3+} was associated with the increase in the number of bridging OH groups, the loading of rhenium carbonyls on TiO_2vac was varied; the same behavior regarding the changes in these bands was observed at several Re loadings (Figure 11.6).

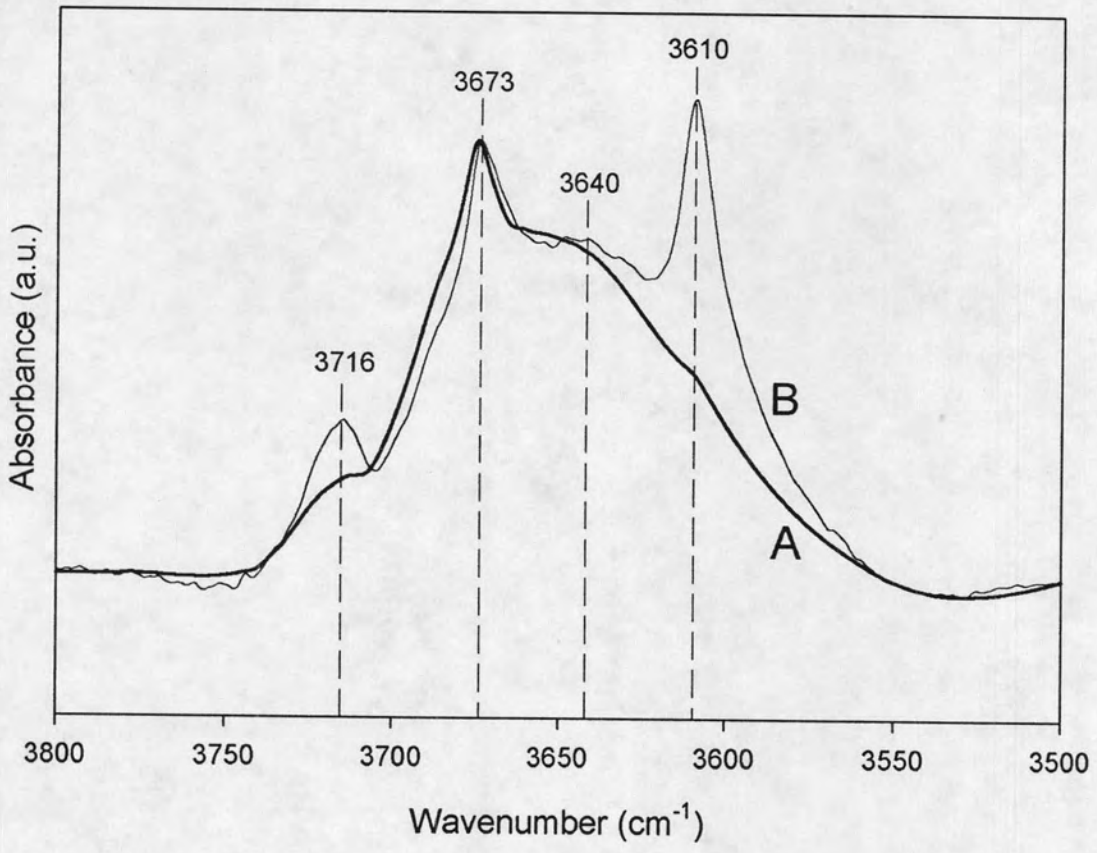

Figure 11.5: Normalized IR spectra in the ν_{OH} region of the samples formed by adsorption of $H_3Re_3(CO)_{12}$ (1.0 wt% Re) on (A) TiO_{2ox} and (B) TiO_{2vac}. Normalization was done by matching the heights of the peaks at approximately 3671 cm^{-1}.

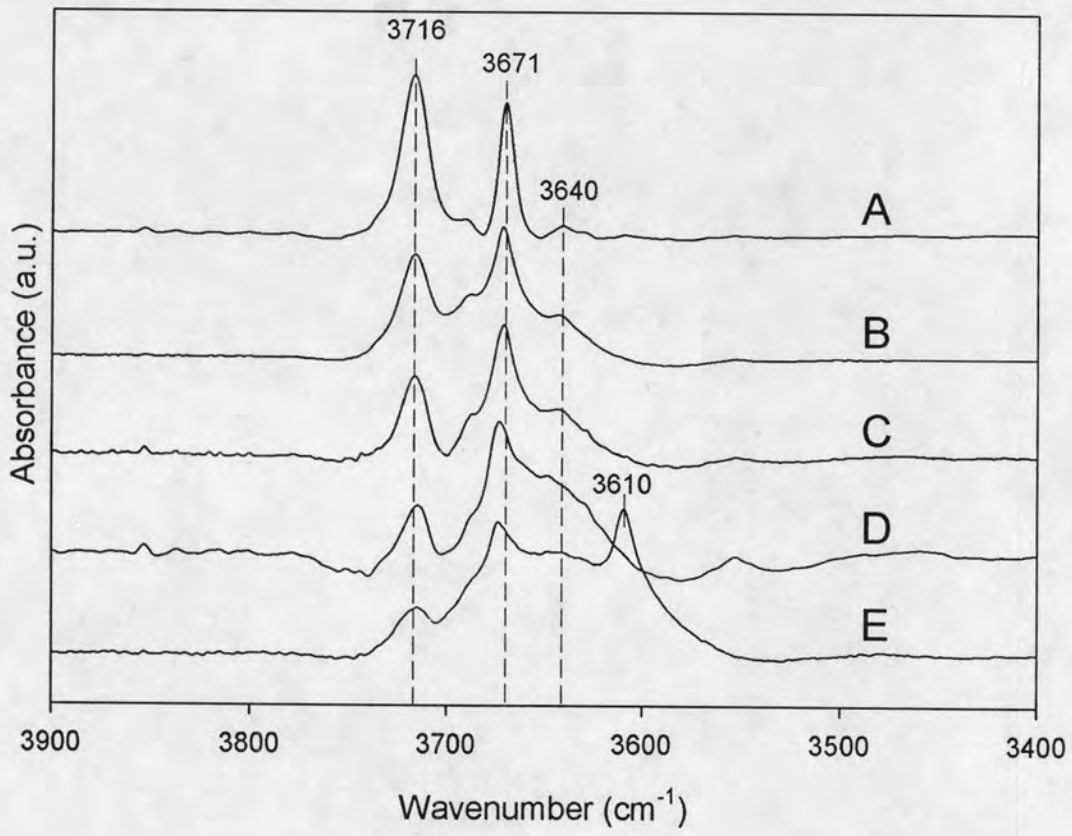

Figure 11.6: Normalized IR spectra in the ν_{OH} region characterizing samples formed by adsorption of $H_3Re_3(CO)_{12}$ on TiO_{2vac} with various Re contents (wt%): A, 0; B, 0.1; C, 0.3; D, 0.6; and E, 1.0. Normalization was done by matching the heights of the peak at approximately 3673 cm^{-1}.

11.6 EPR Evidence of Radical Species on Treated Titania with Adsorbed Rhenium Carbonyls.

There was no influence of *n*-pentane on the EPR signals characterizing either of the treated titania samples, TiO_{2ox} and TiO_{2vac} (Supporting Information), but adsorption of rhenium carbonyls led to changes in the EPR spectra. Adsorption of $H_3Re_3(CO)_{12}$ on the sample treated in O_2 (TiO_{2ox}) (1.0 wt% Re) led to the disappearance of the EPR signals characterizing Ti^{3+}, O_2^-, and O^- (Figure 11.7A). A comparison with the spectrum

of the sample prior to adsorption of the rhenium carbonyl (Figure 7B) shows that the $H_3Re_3(CO)_{12}$ saturated the Ti^{3+} surface defect sites.

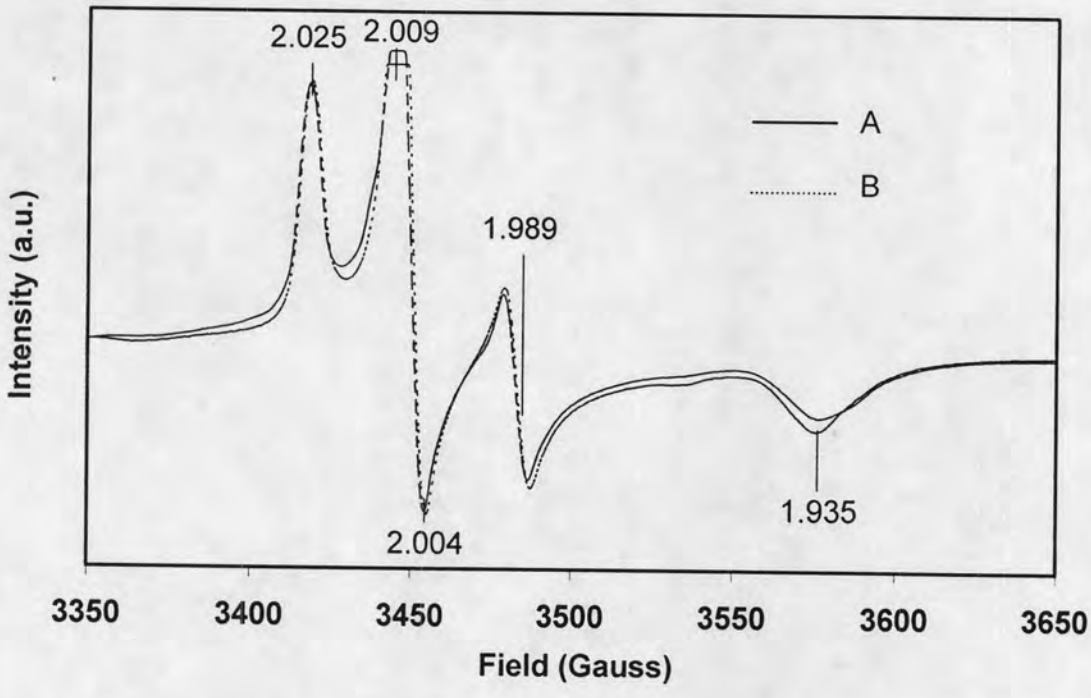

SI 2: EPR spectra of (A) $TiO_{2\ vac}$ and (B) blank $TiO_{2\ vac}$ (titania+ pentane)

The EPR spectrum characterizing the TiO_{2vac} sample containing 1 wt% Re (Figure 11.7C) shows that the signals at g = 1.989 and 1.935 were completely removed upon adsorption of the rhenium carbonyl. Thus, we infer that the adsorbed species completely removed the Ti^{3+} sites on TiO_{2vac}; this behavior matches that observed with TiO_{2ox}. A comparison of the spectrum with that of TiO_{2vac} without adsorbed rhenium carbonyls (Figure 11.7D) shows that the signals at g = 2.004 and 2.009 had been significantly reduced in intensity as a result of the adsorption and that the signal at g = 2.024 was completely removed. Taken together, these results imply that the removal of the O_2^- and O^- species from TiO_{2vac} was incomplete at a Re loading of 1 wt%, in contrast to the observations with the TiO_{2ox} sample containing 1 wt% Re.

Figures 11.7E and C show the EPR spectra of the TiO_{2vac} sample incorporating the lower and higher loadings of rhenium carbonyls (0.1 and 1.0 wt% Re, respectively). A comparison of these spectra with that of TiO_{2vac} without rhenium (Figure 11.7D) shows that the intensity of the EPR spectrum decreased as the rhenium loading increased. Thus, the data show that the Ti^{3+} surface defect sites reacted with—but were not saturated by—the rhenium carbonyls at the lower loading. Correspondingly, the EPR signals indicating oxygen radical species were also observed for the sample containing 0.1 wt% Re (Figure 11.7E).

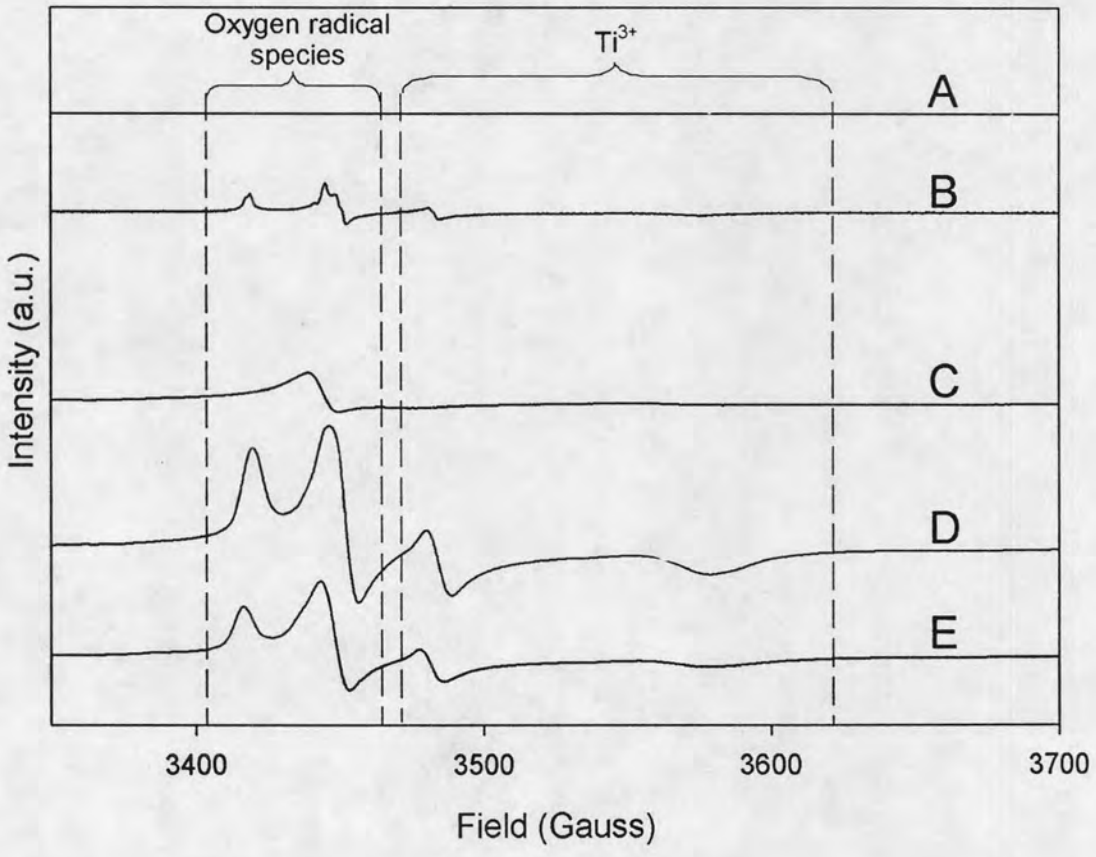

Figure 11.7: EPR spectra of titania and samples formed by adsorption of $H_3Re_3(CO)_{12}$ on titania: A, 1.0 wt% Re on TiO_{2ox}; B, TiO_{2ox}; C, 1.0 wt% Re on TiO_{2vac}; D, TiO_{2vac}; and E, 0.1 wt% Re on TiO_{2vac}.

11.7 EXAFS Data characterizing Rhenium Carbonyls on Treated Titania.

In the EXAFS data analysis, it was found that two models gave good fits of the data characterizing each of the samples incorporating adsorbed rhenium carbonyls—and much better fits than any other that made physical sense. Each successful fit included the following contributions: Re–Re, Re–C, and Re–O, the latter characterized by multiple scattering. The two fits differ in that one includes a Re–O contribution at a longer-than-bonding distance, whereas the other includes a Re–Ti contribution instead. We proceed with these two fits.

The results corresponding to the best fit for each sample according to each model are summarized in Tables 11.5–7, together with errors (precisions, not accuracies) estimated with XDAP [166]. Representative plots of the data and the fits in *k*-space and in *R*-space for the sample containing 1.0 wt% Re on TiO_{2vac} according to the model including a Re–O contribution at a longer-than-bonding distance are shown in Figure 11.8, 11.9, 11.10, 11.11, 11.12, and 11.13; plots for the other samples and models are given in Supporting Information.

Table 11.5: EXAFS Results Characterizing 1.0 wt% Re on TiO_{2ox} Sample[a]

Model and fit parameters	Absorber–backscatterer pair	N_{corr}[a]	N[a]	R[a] (Å)	$\Delta\sigma^2 \times 10^3$ [a] (Å^2)	ΔE_0[a] (Ev)
A	Re–C	3.9 ±0.0	4.0 ±0.0	1.93 ± 0.00	3.2 ±0.1	-3.7 ±0.0
Number of independent points = 25	Re–O[b]	4.3 ±0.0	4.2 ±0.0	3.10 ±0.00	4.1 ±0.2	-0.7 ±0.0
Goodness of fit = 46	Re–Re	2.5 ±0.1	2.3 ±0.1	2.98 ±0.01	7.4 ±0.8	-4.7 ±0.2
$(\chi\nu)^2 = 97$	Re–Ti	0.5 ±0.0	0.5 ±0.0	2.66 ±0.01	3.9 ±0.9	-8.3 ±0.4
B	Re–C	4.1 ±0.0	4.2 ±0.0	1.93 ±0.00	3.5 ± 0.2	-3.6 ±0.1
Number of independent points = 25	Re–O[b]	4.2 ±0.0	4.2 ±0.0	3.10 ±0.00	4.1 ± 0.3	0.4 ±0.1
Goodness of fit = 42	Re–Re	2.4 ±0.1	2.2 ±0.1	2.97 ±0.01	7.3 ± 0.6	-4.5 ±0.3
$(\chi\nu)^2 = 75$	Re–O	1.5 ±0.0	1.2 ±0.0	2.59 ±0.01	4.7 ± 1.0	-9.8 ±0.3

[a] Notation: N, coordination number; N_{corr}, is the coordination number corrected for the mean free path of the electron; R, distance between absorber and backscatterer atoms; $\Delta\sigma^2$, Debye-Waller factor relative to reference material; and ΔE_0, inner potential correction.

[b]Re–O contribution characterized by co-linear multiple scattering of the group Re–C–O
The mean free path was taken as 6 Å. The k- and R- ranges were 2.71–11.74 Å^{-1} and 0.5–4.0 Å. The number of independent points where 22

All interval reported in this table correspond to precisions associated to the fit.. The accuracies associated to the model parameters are for the metal shell: N: ±10%, R: ±0.02 Å, $\Delta\sigma^2$: ±20%, ΔE_0,: ±20%, and for light scatterers: N: ±20%; R: ±0.02 Å; $\Delta\sigma^2$: ±20%; ΔE_0: ±20%.

Table 11.6: EXAFS Results Characterizing 1.0 wt% Re on TiO_{2vac}[a]

Model and fit parameters	Absorber–backscatterer pair	N_{corr}[a]	N[a]	R[a] (Å)	$\Delta\sigma^2 \times 10^3$ [a], (Å^2)	ΔE_0[a] (Ev)
A	Re–C	3.6 ± 0.0	3.7 ± 0.0	1.95 ± 0.00	3.2 ± 0.1	-4.8 ± 0.0
Goodness of fit = 34	Re–O[b]	4.5 ± 0.0	4.5 ± 0.0	3.09 ± 0.00	4.9 ± 0.1	0.0 ± 0.0
$(\Delta\sigma)^2$ = 42	Re–Re	1.7 ± 0.1	1.6 ± 0.1	2.93 ± 0.00	3.0 ± 0.3	11.1 ± 0.5
	Re–Ti	0.4 ± 0.0	0.4 ± 0.0	2.62 ± 0.01	5.9 ±1.0	1.3 ± 0.6
B	Re–C	3.7 ±0.0	3.8 ± 0.0	1.95 ± 0.0	3.2 ± 0.1	-4.7 ± 0.0
Goodness of fit = 20	Re–O[b]	4.3 ± 0.0	4.2 ± 0.0	3.13 ± 0.0	6.4 ± 0.1	-0.8 ± 0.0
$(\Delta\sigma)^2$ = 22	Re–Re	2.3 ± 0.1	2.2 ± 0.1	2.94 ± 0.0	5.0 ± 0.4	-3.8 ± 0.2
	Re–O	1.4 ± 0.0	1.1 ± 0.0	2.57 ± 0.0	7.5 ± 0.6	-8.2 ± 0.1

[a] Notation: N, coordination number; N_{corr}, is the coordination number corrected for the mean free path of the electron; R, distance between absorber and backscatterer atoms; $\Delta\sigma^2$, Debye-Waller factor relative to reference material; and ΔE_0, inner potential correction.

[b]Re–O contribution characterized by co-linear multiple scattering of the group Re–C–O

The mean free path was taken as6 Å. The k- and R- ranges where 2.72–11.74 Å^{-1} and 0.5–4 Å. The number of independent points where 22

All interval reported in this table correspond to precisions associated to the fit.. The accuracies associated to the model parameters are for the metal shell: N: ±10%, R: ±0.02 Å, $\Delta\sigma^2$: ±20%, ΔE_0,: ±20%, and for light scatterers: N: ±20%; R: ±0.02 Å; $\Delta\sigma^2$: ±20%; ΔE_0: ±20%.

Table 11.7: EXAFS Results Characterizing 0.1% Re on TiO_{2vac}[a]

Model and fit parameters	Absorber–backscatterer pair	N_{corr}[a]	N[a]	R[a] (Å)	$\Delta\sigma^2 \times 10^3$ [a] (Å^2)	ΔE_0[a] (Ev)
A	Re–C	3.9 ± 0.0	4.1 ± 0.0	1.81 ± 0.0	7.8 ± 0.0	0.6 ± 0.1
Goodness of fit = 11	Re–O[b]	4.2 ± 0.0	4.2 ± 0.0	3.11 ± 0.0	11.0 ± 0.3	-1.1 ± 0.0
$(\Delta\sigma)^2$ = 29	Re–Re	2.3 ± 0.1	2.2 ± 0.1	2.90 ± 0.00	4.2 ± 0.6	0.8 ± 0.3
	Re–Ti	0.7 ± 0.0	0.7 ± 0.0	2.60 ± 0.01	5.9 ± 1.0	-8.8 ± 0.4
B	Re–C	4.0 ± 0.0	4.2 ± 0.0	1.81 ± 0.00	8.1 ± 0.2	1.1 ± 0.1
Goodness of fit = 11	Re–O[b]	3.9 ± 0.0	3.8 ± 0.0	3.13 ± 0.00	11.5 ± 0.3	-1.6 ± 0.1
$(\Delta\sigma)^2$ = 30	Re–Re	2.2 ± 0.1	2.1 ± 0.1	2.86 ± 0.00	2.2 ± 0.5	9.6 ± 0.3
	Re–O	1.4 ± 0.0	1.2 ± 0.1	2.49 ± 0.00	7.3 ± 0.9	-1.1 ± 0.2

[a] Notation: N, coordination number; N_{corr}, is the coordination number corrected for the mean free path of the electron; R, distance between absorber and backscatterer atoms; $\Delta\sigma^2$, Debye-Waller factor relative to reference material; and ΔE_0, inner potential correction.

[b]Re–O contribution characterized by co-linear multiple scattering of the group Re–C–O

The mean free path was taken as 6 Å. The k- and R- ranges where 2.68–10.42 Δ^{-1} and 0.5–4 Δ. The number of independent points where 19

All interval reported in this table correspond to precisions associated to the fit. The accuracies associated to the model parameters are for the metal shell: N: ±10%, R: ±0.02 Å, $\Delta\sigma^2$: ±20%, ΔE_0,: ±20%, and for light scatterers: N: ±20%; R: ±0.02 Å; $\Delta\sigma^2$: ±20%; ΔE_0:±20%.

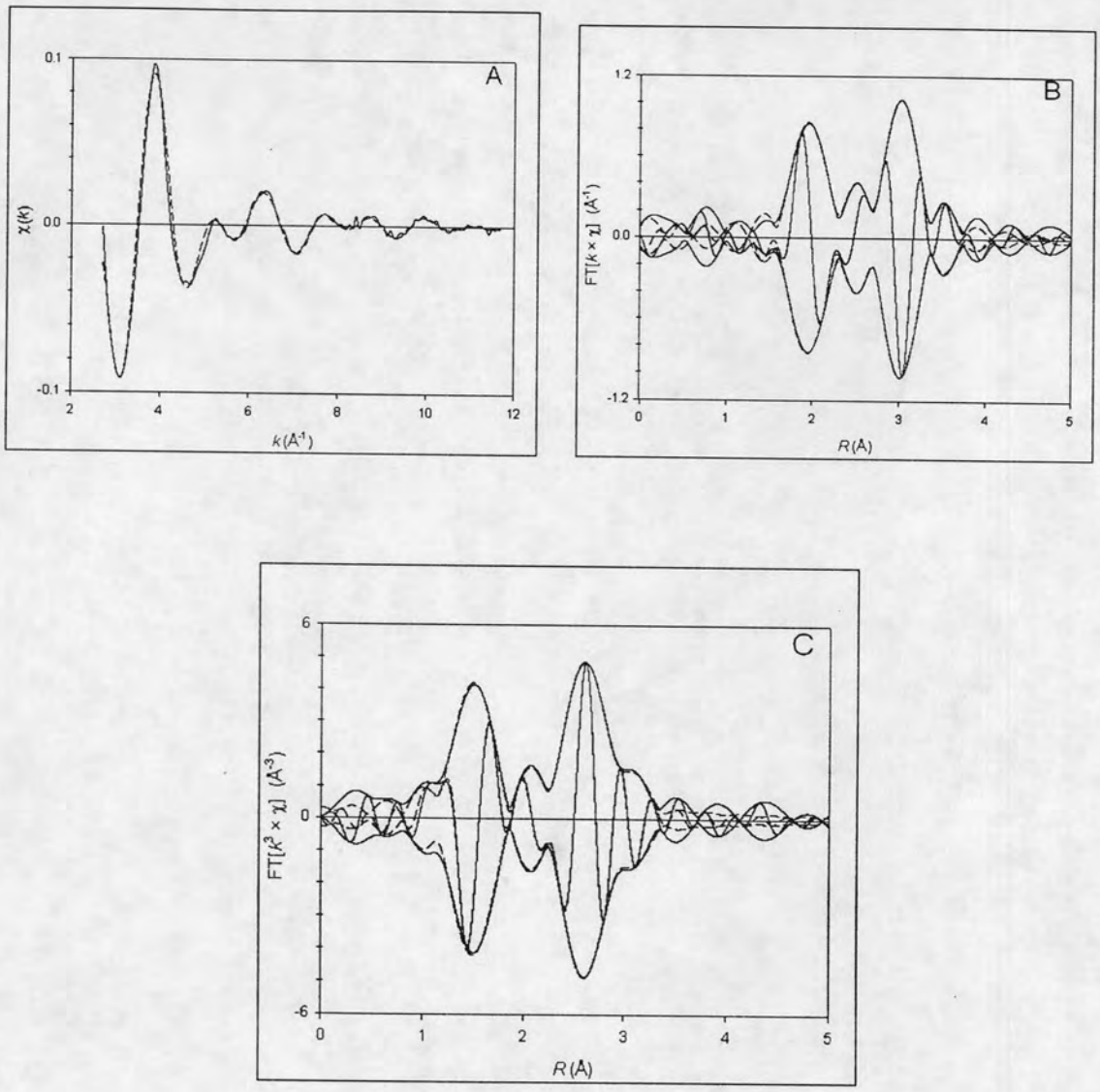

Figure 11.8: EXAFS data characterizing sample formed from $H_3Re_3(CO)_{12}$ and TiO_{2ox} containing 1.0 wt% Re. Data, continuous line, and model incorporating Re–O contribution at R = 2.59 Å, broken line. A, k^0-weighted EXAFS function in k-space; B, imaginary part and magnitude of k^1-weighted EXAFS function in R-space; and C, imaginary part and magnitude of k^3-weighted EXAFS function in R-space.

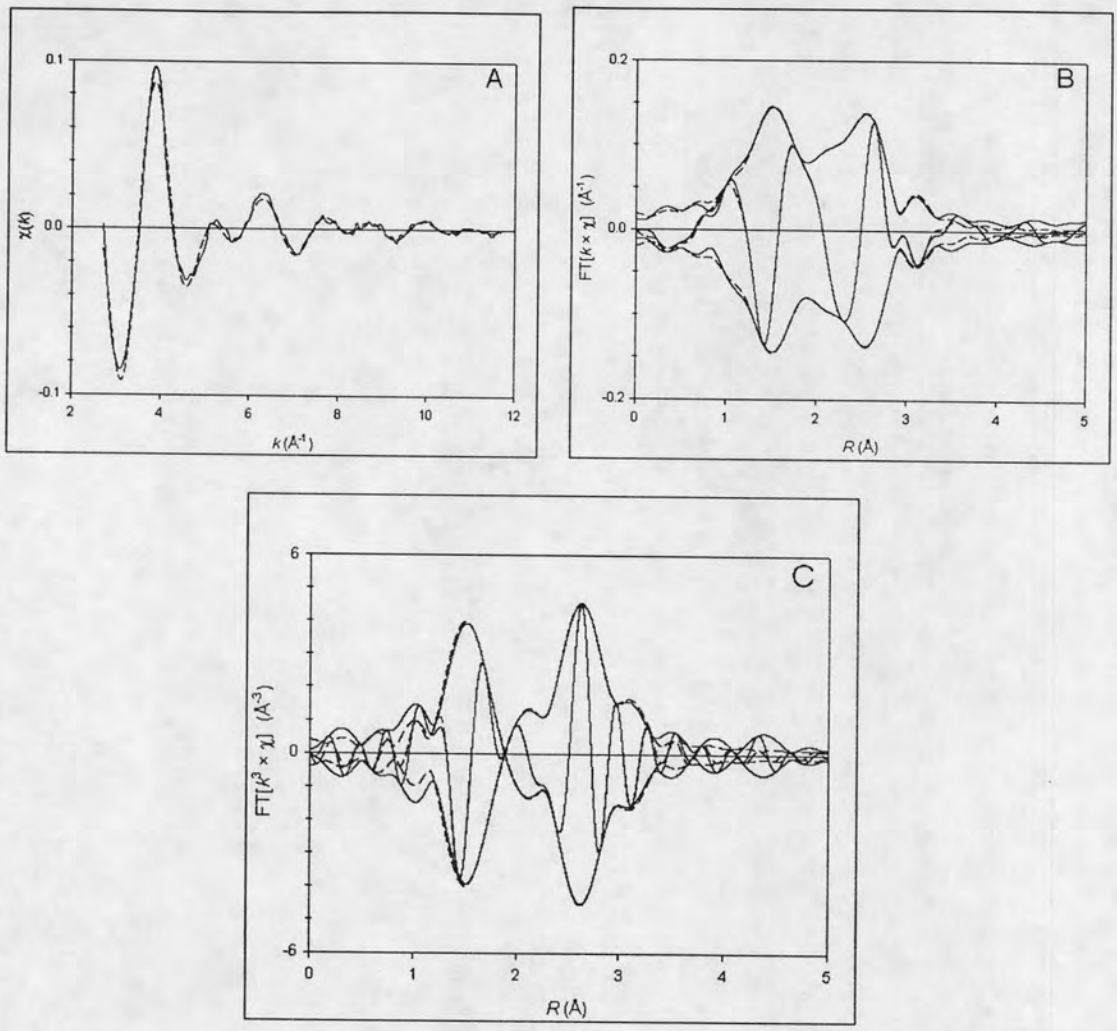

Figure 11.9: EXAFS data characterizing sample formed from $H_3Re_3(CO)_{12}$ and TiO_{2vac} with 1 wt% Re. Experimental results, continuous line, and model containing Re–O contribution at $R = 2.57$ Å, broken line. A, k^0-weighted EXAFS function in k-space; B, imaginary part and magnitude of k^1-weighted EXAFS function in R-space; and C, imaginary part and magnitude of k^3-weighted EXAFS function in R-space.

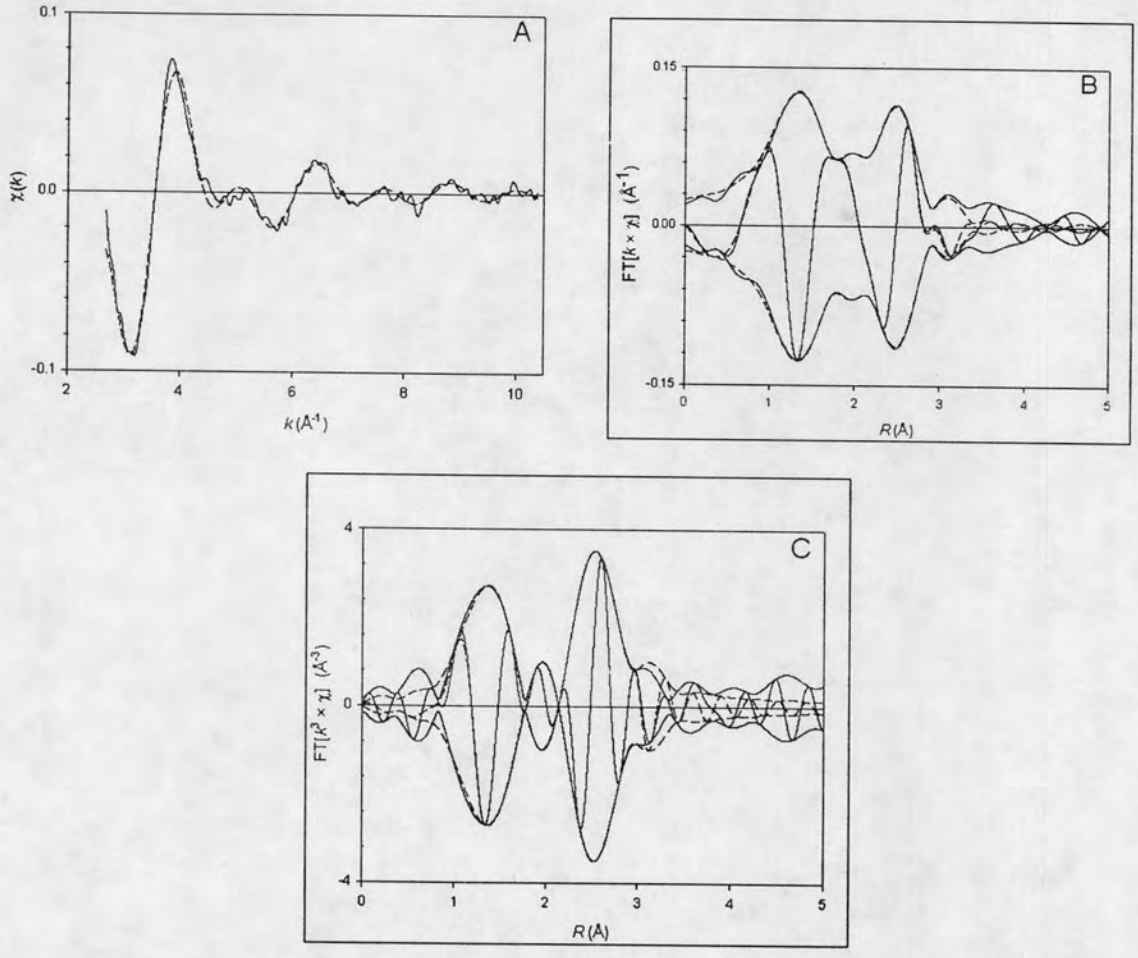

Figure 11.10: EXAFS data characterizing sample formed from $H_3Re_3(CO)_{12}$ and TiO_{2vac} with 0.1 wt% Re. Experimental results, continuous line, and model containing Re–O contribution at $R = 2.49$ Å, broken line. A, k^0-weighted EXAFS function in k-space; B, imaginary part and magnitude of k^1-weighted EXAFS function in R-space; and C, imaginary part and magnitude of k^3-weighted EXAFS function in R-space.

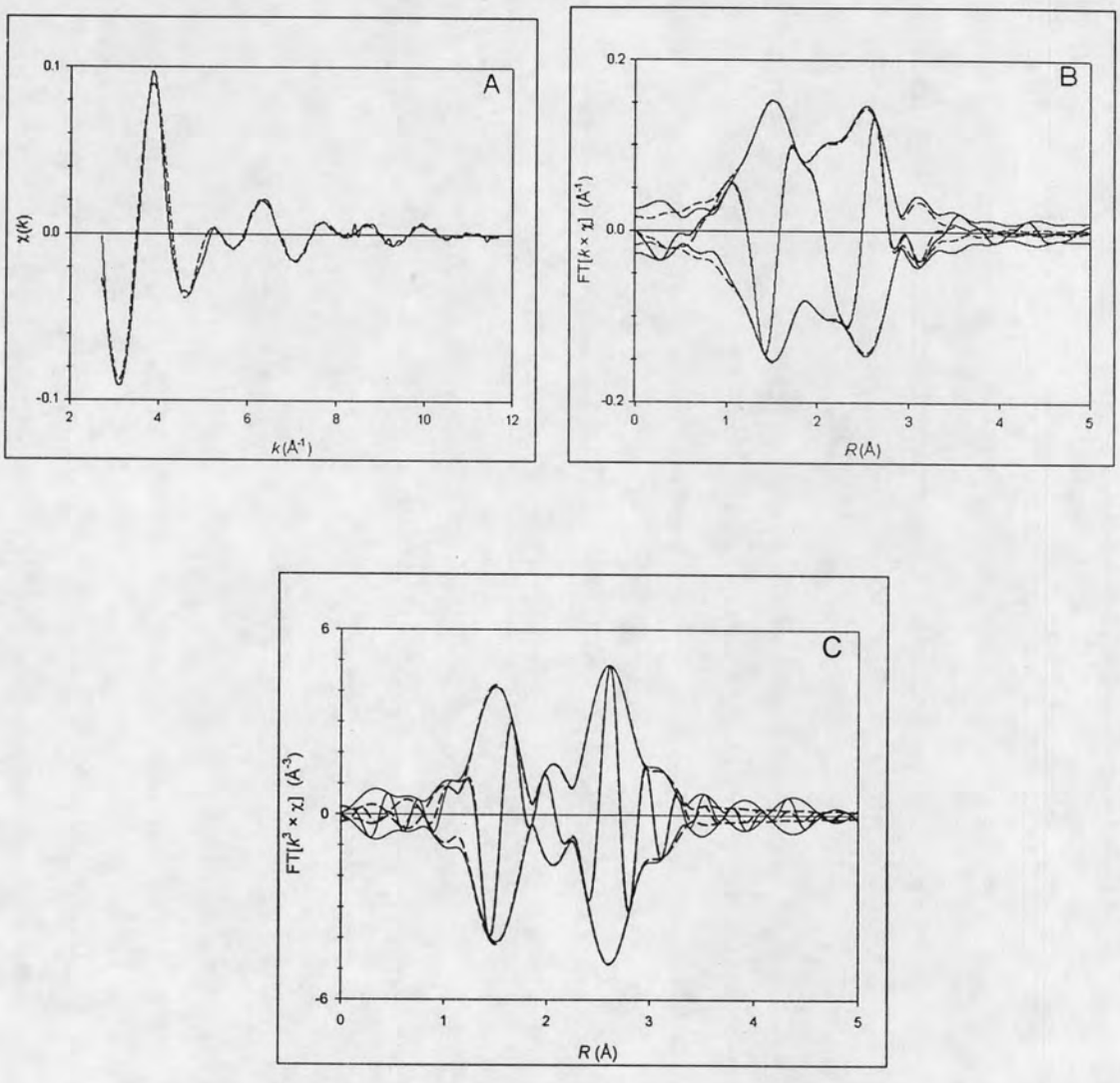

Figure 11.11: EXAFS data characterizing sample formed from $H_3Re_3(CO)_{12}$ and TiO_{2ox} with 1 wt% Re. Experimental results, continuous line, and model containing Re–Ti contribution at R = 2.49 Å, broken line. A, k^0-weighted EXAFS function in k-space; B, imaginary part and magnitude of k^1-weighted EXAFS function in R-space; and C, imaginary part and magnitude of k^3-weighted EXAFS function in R-space.

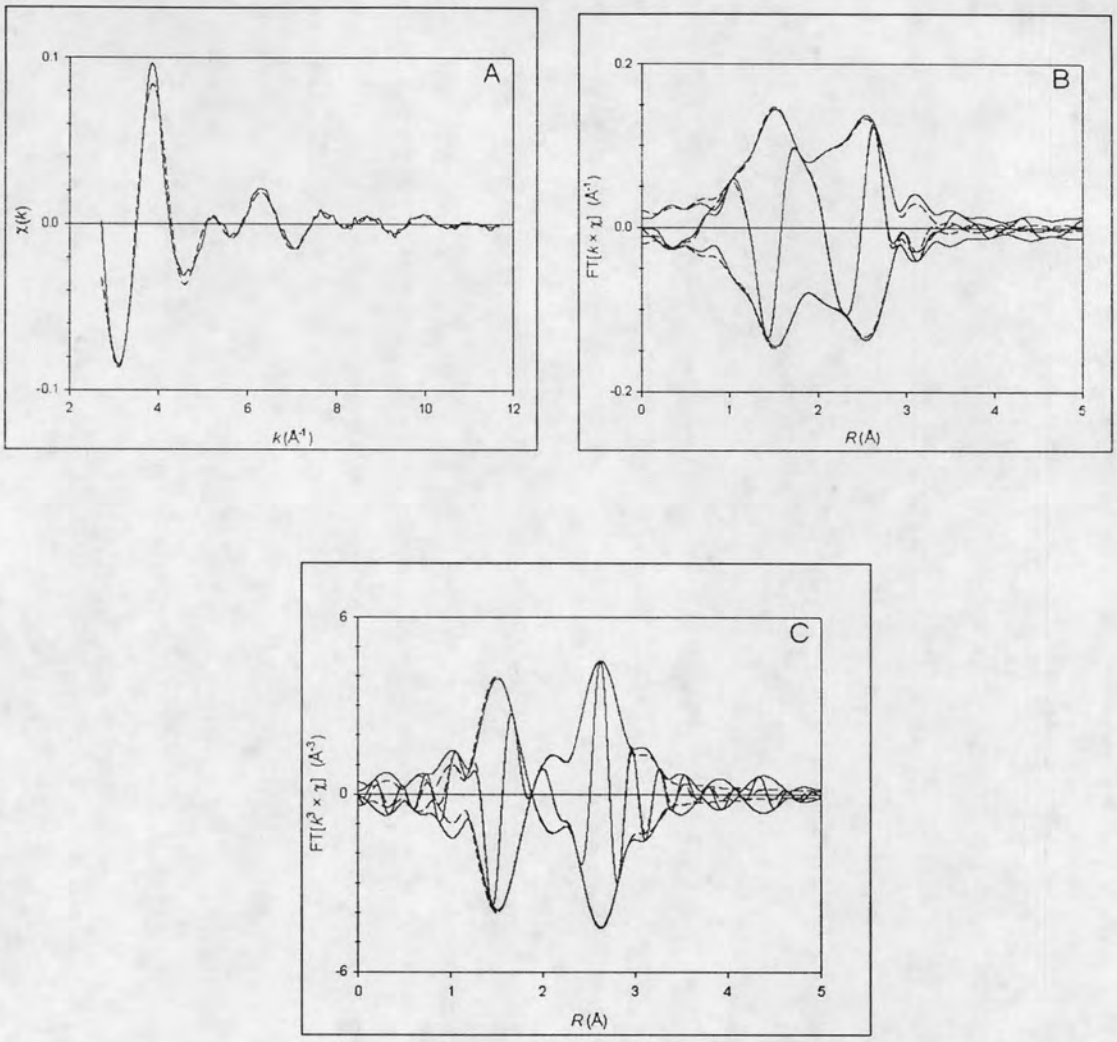

Figure 11.12: EXAFS data characterizing sample formed from $H_3Re_3(CO)_{12}$ and TiO_{2vac} with 1 wt% Re. Experimental results, continuous line, and model containing Re–Ti contribution at R = 2.49 Å, broken line. A, k^0-weighted EXAFS function in k-space; B, imaginary part and magnitude of k^1-weighted EXAFS function in R-space; and C, imaginary part and magnitude of k^3-weighted EXAFS function in R-space.

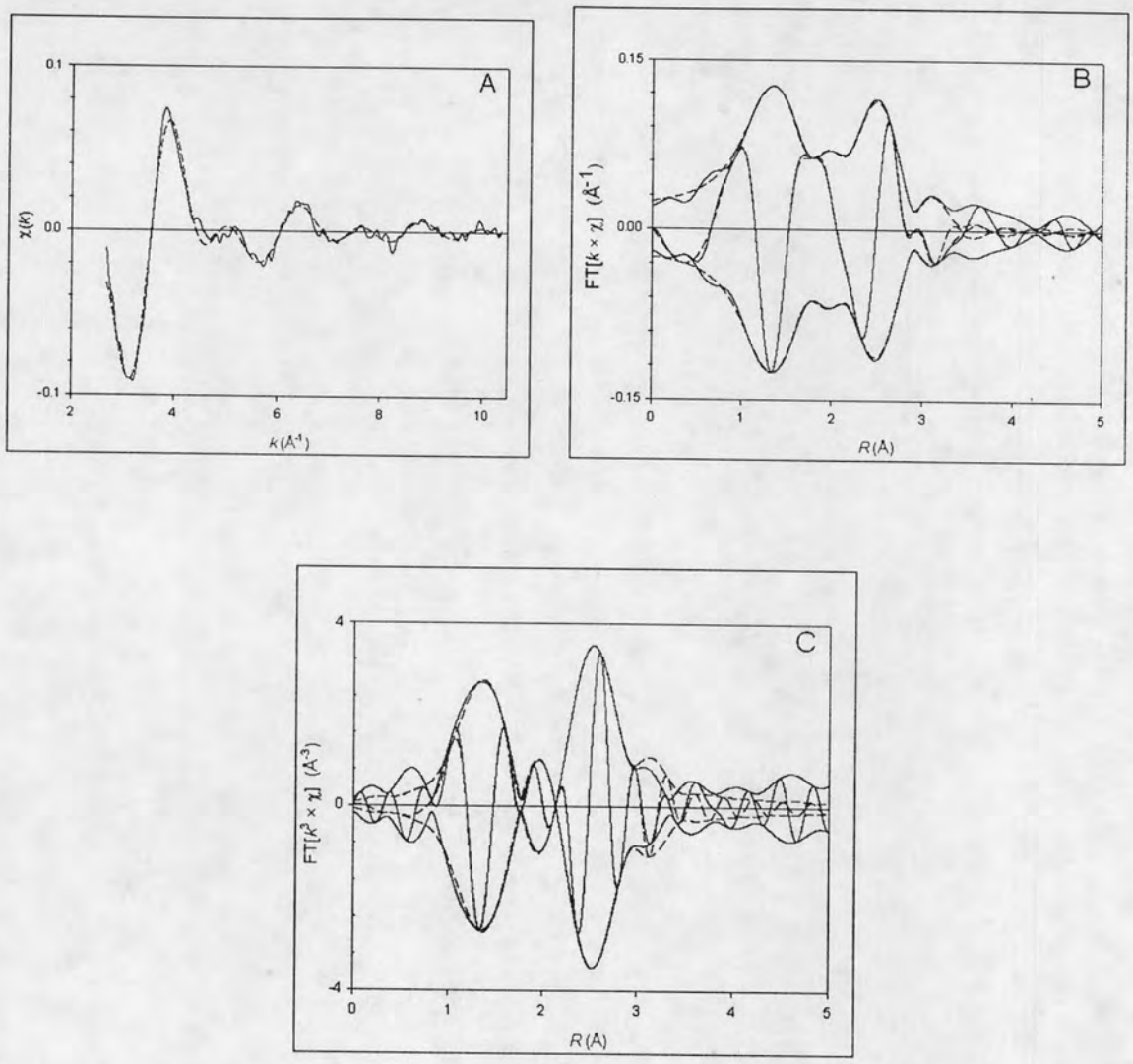

Figure 11.13: EXAFS data characterizing sample formed from $H_3Re_3(CO)_{12}$ and TiO_{2vac} with 0.1 wt% Re. Experimental results, continuous line, and model containing Re–Ti contribution at R = 2.49 Å, broken line. A, k^0-weighted EXAFS function in k-space; B, imaginary part and magnitude of k^1-weighted EXAFS function in R-space; and C, imaginary part and magnitude of k^3-weighted EXAFS function in R-space.

11.7.1 Sample incorporating 1.0 wt% Re on TiO_{2ox}.

The model representing the sample containing 1.0 wt% Re on TiO_{2ox} includes a Re–Re contribution with a coordination number of nearly 2 at distances of 2.98 □ for one model (designated model A) and 2.97 □ for another (designated model B). The coordination number indicates that the trirhenium frame remained essentially intact upon adsorption of the clusters. The Re–Re distance in the adsorbed clusters is significantly shorter than that in crystalline $H_3Re_3(CO)_{12}$ (3.28 □) and closer to that in the anion $[H_2Re_3(CO)_{12}]^-$ [167]. The comparison suggests that the rhenium carbonyls were deprotonated upon adsorption on TiO_{2ox}, consistent with the basicity of the surface [168].[Error! Reference source not found.]

The Re–C and Re–O contributions in each model are characterized by multiple scattering (as expected for linear Re–C–O moieties), with Re–C and Re–O distances of 1.93 and 3.10 Å, respectively, consistent with carbonyl ligands bonded to rhenium [167]. The Re–C and Re–O coordination number found for each model (approximately 4) corresponds to the Re:CO ratio of the precursor $H_3Re_3(CO)_{12}$ and indicates the lack of decarbonylation of the clusters upon adsorption, consistent with the ν_{CO} spectra.

The key difference between the two models is that one includes a Re–O contribution other than the Re–carbonyl-oxygen contribution and the other instead includes a Re–Ti contribution; the respective Re–O and Re–Ti distances are 2.59 and at 2.66 □, and the respective coordination numbers are 1.5 and 0.5. The coordination number and length of the Re–O contribution in the former model are in agreement with other observations [169]; They would be expected to depend on the surface site geometry and possible distortion of the carbonyl ligands on the cluster. The parameters characterizing the Re–Ti contribution in the latter model are also plausible. The goodness of fit is better for the former model—and the value of $(□□)^2$ is smaller—and thus we prefer this model.

11.7.2 Sample incorporating 1.0 wt% Re on TiO_{2vac}.

As for the sample containing 1% Re on TiO_{2ox}, the two models representing the EXAFS data characterizing the sample that had been treated in vacuum each incorporate a Re–Re contribution with a coordination number of 2, within error, at a distance of 2.93 □ for model A and 2.94 □ for model B; these are significantly shorter than the distance observed for $H_3Re_3(CO)_{12}$ (3.24 Å) [167]. As for the sample prepared from TiO_{2ox}, this distance agrees better with a Re–Re distance characteristic of deprotonated clusters than of $H_3Re_3(CO)_{12}$.

Again, as for the sample containing 1 wt % Re on TiO_{2ox}, the EXAFS data indicate the presence of carbonyl ligands (a Re–C and a Re–O contribution characterized by multiple scattering) with a coordination number of approximately 4, at distances of 1.95 and 3.09 □ for model A and 1.95 and 3.13 □ for model B, respectively, consistent with the inference that the rhenium clusters were not substantially decarbonylated upon adsorption, and in agreement with observations of adsorption of $H_3Re_3(CO)_{12}$ on other metal oxides [170].

The distances of the Re–O and Re–Ti contributions in the two models are 2.57 and 2.62 □, and the respective coordination numbers are 1.4 and 0.4. These parameters match those observed for the sample containing 1 wt % Re on TiO_{2ox}, and the model including the Re–O contribution gave a far better fit than the one with a Re–Ti contribution, as judged by the goodness of fit and the value of $(□□)^2$ (which respectively are 33 and 48% lower for the model with the Re–O contribution than for the other).

11.7.3 Sample incorporating 0.1 wt% Re on TiO_{2vac}.

The quality of the EXAFS data characterizing the sample with the low Re content (0.1 wt%) on TiO_{2vac} is lower than that of the other samples, but it was good enough for a satisfactory data analysis. The goodness of fit and $(□□)^2$ criteria do not provide a basis for distinguishing between the two models (Table 7). We tentatively

prefer the model incorporating the Re–O rather than the Re–Ti contribution on the basis of an assumed analogy with the samples with the higher rhenium loading.

As for the samples containing 1.0 wt% Re, both of the models providing a good fit include a Re–Re contribution with a coordination number of nearly 2. However, the models apparently differ slightly from each other in that the Re–Re distances are 2.86 and 2.90 □ for the models including the Re–O and Re–Ti contributions, respectively (but the difference in the Re–Re distances almost matches the uncertainty in the values). According to the model including the Re–O contribution, this distance is significantly shorter than that observed for the samples containing 1% Re on either TiO_{2vac} or TiO_{2ox}. This result suggests that the Re–Re bond was strengthened upon adsorption of the cluster at the low loading (at the Ti^{3+} defect site). In the model with the Re–Ti contribution, the differences between the parameters and those characterizing the sample incorporating 1.0 wt% Re are too small to resolve.

In both models of the sample containing 0.1 wt% Re, Re–C and Re–O contributions characterized by multiple scattering were observed, with a coordination number of 4 for each shell, and distances of 3.11 and 3.13 Å for models A and B, respectively, for the Re–O contribution, matching that observed for the samples containing 1.0 wt% Re. In contrast, a Re–C distance of 1.81 □ was observed for both models characterizing the sample containing only 0.1% Re on TiO_{2vac}; this distance is more than 0.12 □ shorter than that found for the samples containing 1.0 wt% Re on either titania sample. This comparison suggests that the Re–C bonds were stronger in the former sample than in the latter. Furthermore, this distance is closer to that observed [171] For $[Hre_3(CO)_{12}]^{2-}$, which suggests that a greater degree of cluster deprotonation was achieved in this sample, in which the clusters were bonded at Ti^{3+} defect sites.

According to the fit for the model including a Re–Ti contribution, this contribution is characterized by a coordination number of 0.7 at a distance of 2.60 □. These values match, within error, those determined for the two samples containing 1.0 wt% Re for the same model.

According to the fit for the model including a Re–O contribution, this contribution is characterized by a coordination number of 1.4 at a distance of 2.49 □. The latter value is significantly shorter than that observed for the two samples containing 1.0 wt% Re and therefore indicates a stronger interaction of the metal clusters with the support in the sample with the low rhenium loading than in the samples with the high rhenium loading.

In summary, according to either model, a strong interaction of the clusters with the support is indicated, and in the model with the Re–O and not the Re–Ti contribution the data distinguish a stronger cluster–support interaction than for the samples containing 1.0 wt% Re.

11.8 Formation of Defect Sites on Titania

The data reported here are consistent with the literature in demonstrating that treatment of titania under vacuum at 723 K leads to the formation of defects identified as Ti^{3+} at oxygen vacancy sites on the surface (Figures 11.2 and 11.3). Formation of a surface defect site has been explained as the result of removing a lattice oxygen atom and one electron during the treatment, with one electron being left in the d orbital of the neighboring surface Ti site [172], So that Ti^{4+} is reduced to Ti^{3+}.

The IR spectra show that surface OH groups associated with the defect sites were formed as bridging OH groups incorporating bridging lattice oxygen atoms were removed (Figure 11.3), generating surface defect sites and oxygen radical species (as demonstrated by EPR spectroscopy, Figure 11.2). These results are the first demonstration that the formation of the defect sites and oxygen radicals on titania is accompanied by the disappearance of bridging OH groups and the formation of OH groups associated with the defect sites.

Thus, the results show how EPR and IR spectroscopies complement each other for characterization of this titania surface chemistry; they also go beyond those reported in the use of a metal carbonyl as a surface probe, as discussed below.

There are two types of lattice oxygen on the most stable (110) single-crystal rutile surface, bridging and in-plane lattice oxygen [173]. STM images show that the twofold-coordinated bridging lattice oxygen is removed more easily than the threefold-coordinated in-plane lattice oxygen [174], And removal of the former can even eliminate entire rows of rutile oxygen atoms during treatment under vacuum [175].

There is a lack of such information for anatase, but, on the basis of the aforementioned STM results and the fact that the predominant face of anatase is the (101) [176,177,178,179] (which is similar to the (110) face of rutile—having the same 5-fold and 6-fold coordinated Ti atoms and the same two-fold and three-fold coordinated oxygen atoms, but at different angles), we suggest that the formation of surface defect sites (Ti^{3+}) on our TiO_{2vac} (anatase) sample likely resulted from the removal of bridging lattice oxygen atoms. This suggestion is consistent with (a) IR spectra showing the removal of bridging OH groups as defect sites are formed and (b) theoretical results [180] showing how water adsorbs on the (101) face of anatase after removal of bridging oxygen atoms.

Our EPR data show that, after removal of lattice oxygen, some oxygen remained on the titania surface in the form of either O_2^- or O^- (Figure 11.2). Because no increase in the intensity of the EPR peaks indicative of O_2^- and O^- was observed when the sample was treated in O_2 (to prepare TiO_{2ox}), we infer that these radical species did not form from O_2, but instead from lattice oxygen, as has been suggested by Howe et al.

11.9 Schematic Representation of Formation of Defects on Titania Surface

On the basis of the EPR and IR results, we propose a simplified representation (Scheme 11.1) to explain the changes in the surface resulting from treatment under vacuum. This model is proposed for the predominant anatase (101) surface. The scheme represents the hydroxylated surface before and after the treatments, as characterized by EPR and IR spectroscopies.

As shown in Scheme 11.1, the surface of the untreated titania incorporates relatively few Ti^{3+} sites and O_2^- and O^- species—as shown by the relatively low-intensity EPR signals. This surface also incorporates a low density of Ti^{3+}–OH groups (ν_{OH} = 3716 cm^{-1}) and a relatively high density of bridging OH groups (ν_{OH} = 3643 cm^{-1}) (Figure 3).

Treatment of this sample under vacuum (giving TiO_{2vac}) led to an increase in the number of Ti^{3+} sites (g = 1.989 and 1.935, Figure 11.2C) and a simultaneous increase in the number of Ti^{3+}–OH groups (ν_{OH} = 3716 cm^{-1}, Figure 11.3C). We postulate that these changes are initiated on Ti^{4+} sites incorporating OH groups, as the bond between a bridging lattice oxygen and a Ti^{4+} ion is broken and an O^- species is formed, leading to a conversion of a Ti^{4+} into a Ti^{3+} site and correspondingly of Ti^{4+}–OH into Ti^{3+}–OH groups (Scheme 11.1A). We also postulate that the formation of an O^- radical species (indicated by the increased intensity of the EPR signals, Figure 11.2) is associated with the breaking of a bond between Ti^{4+} and a bridging lattice oxygen atom (Scheme 11.1B).

Treatment of titania under vacuum also led to a decrease in the number of bridging OH groups (ν_{OH} = 3640 cm^{-1}) and a simultaneous increase in the number of Ti^{3+}–OH groups (ν_{OH} = 3716 cm^{-1}) (Figure 11.3). We postulate that these changes resulted from the removal of bridging OH groups and the simultaneous conversion of Ti^{4+}–OH into Ti^{3+}–OH groups (Scheme 11.1B). We also infer that the formation of O_2^- species characterized by EPR (Figure 2C, g = 2.025, 2.009, and 2.004) results from removal of bridging lattice oxygen atoms (Scheme 11.1C), but the mechanism of this reaction remains unclear. The plausibility of this inference is supported by calculations at

the level of density functional theory showing that a minimum-energy configuration corresponds to an O_2^- species located at a five-fold coordinated Ti^{4+} site (Scheme 11.1).

In summary, the simplified representation shown in Scheme 11.1 is consistent with both the EPR and IR data and explains the formation of surface Ti^{3+} defect sites; it is broadly consistent with the literature and specifically with the more restricted representation of Tilocca and Selloni [180], Which however does not involve OH groups in the formation of defect sites. Their representation instead accounts for OH groups resulting from the dissociation of water on the defect sites—and experimental evidence of such OH group formation has been presented by Henderson [168].

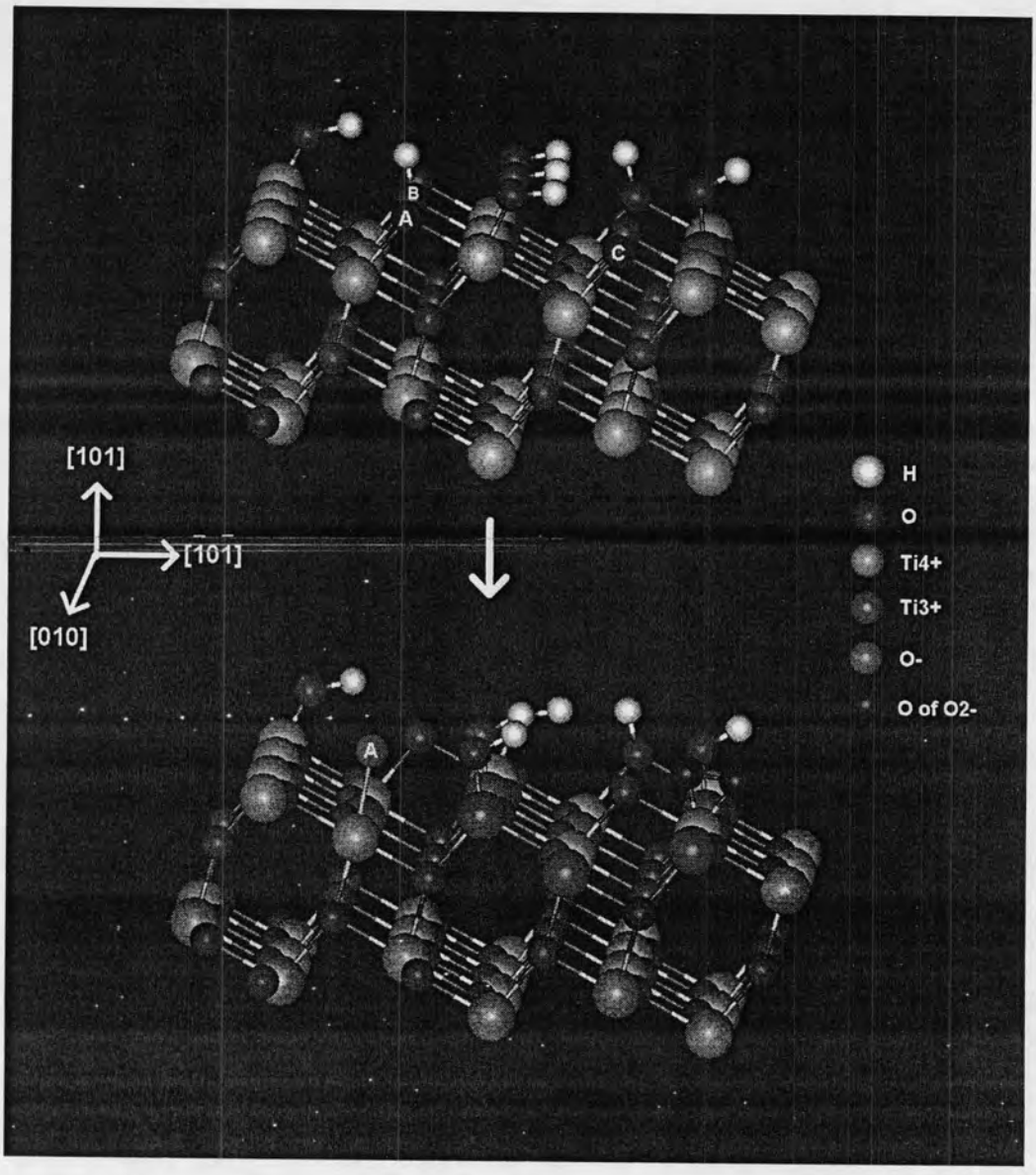

Scheme 11.1: The model representing the surface of anatase before and after treatment

11.10 Probing Titania Defect Sites with Rhenium Carbonyl Clusters

Both TiO_{2vac} and TiO_{2ox} lost Ti^{3+} surface defect sites (g = 1.989 and 1.935) when the rhenium carbonyl was adsorbed, as demonstrated by the EPR spectra (Figure 11.7). This change was accompanied by a decrease in the density of Ti^{3+}–OH groups (3716 cm^{-1}, Figure 11.5). These results might be explained by either of two mechanisms: (a) rhenium carbonyl clusters bonded to Ti^{3+} sites and accepted lone-pair electrons from d

orbitals of Ti^{3+}, leading to the formation of Re–Ti bonds, or (b) rhenium carbonyl clusters healed the surface defects (Ti^{3+}) at oxygen vacancy sites, transforming Ti^{3+} into Ti^{4+} sites.

The former mechanism is inconsistent with the EPR results, because, if it had occurred, it would have led to a hyperfine pattern of six peaks in the EPR spectrum arising from the interaction between lone-pair electrons ($S = \pm 1/2$) of Ti^{3+} sites and the ^{187}Re nucleus with $I = \pm 5/2$, with a natural abundance of 62.7% [181]. Thus, we discount the former mechanism and also the EXAFS model including a Re–Ti contribution—in line with its giving a poorer fit of the data representing the two samples with the higher Re loading.

The IR results (Figure 11.5) show that, after adsorption of $H_3Re_3(CO)_{12}$, especially on TiO_{2vac}, the bridging OH groups became evident and the density of the Ti^{3+}–OH groups and surface defects (Ti^{3+}) decreased (Figure 11.7), consistent with the suggestion of a process of healing of the defect sites by the rhenium carbonyls. Thus, the data show how the rhenium carbonyl is an informative probe of the chemistry of the Ti^{3+} surface defect sites.

The IR and EPR spectra are both sensitive to the loading of rhenium carbonyls on the surface (Figures 11.6 and 11.7). When the loading of Re on the surface was only 0.1 wt%, the EPR signal characteristic of Ti^{3+} was not fully removed, which implies that the defect sites were not saturated at this loading. Consistent with this result, the IR spectra (Figure 11.6B) show that the OH band associated with the Ti^{3+} sites was not completely removed. Thus, we work from the hypothesis that all the rhenium on the surface at this low loading was present at the defect sites and infer that with more precise and systematic experimentation, it would be possible to refine the methods to count the number of the defect sites by titrating them with $H_3Re_3(CO)_{12}$. We caution that EPR, IR, and EXAFS data in combination would be required to distinguish the rhenium carbonyls in the defect from those present at other sites.

Thus, the EXAFS data characterizing the rhenium carbonyls at the lower loading are different from those characterizing the rhenium carbonyls at the higher loading. Specifically, the former are characterized by a shorter Re–O distance indicating a stronger interaction of the clusters with the support than in the case of the higher rhenium loading. Furthermore, the Re–C and C–O distances characterizing the clusters present at the lower loading are close to those reported for $[Hre_3(CO)_{12}]^{2-}$ (Table 11.8), and the values are markedly different from those characterizing the rhenium carbonyls at the higher loading, which correspond to less deprotonated clusters (Table 11.8) [167,171].

Table 11.8: Comparison of Re–C and C–O Bond Distances in the $[H_xRe_3(CO)_{12}]^{x-3}$ (x = 1 – 3) and in the Supported Rhenium Carbonyls.

Cluster	Bond distance (Å)		Ref.
	Re–C	C-O	
$[H_3Re_3(CO)_{12}]$	1.98	1.13	
$[H_2Re_3(CO)_{12}]^-$	1.92	1.18	
$[Hre_3(CO)_{12}]^{2-}$	1.83	1.24	
1% Re on TiO_{2ox} (model B)	1.93	1.17	This work
1% Re on TiO_{2vac} (model B)	1.95	1.18	This work
0.1% Re on TiO_{2vac} (model B)	1.81	1.32	This work

In summary, the data show the rhenium clusters present at the lower loading of 0.1 wt% Re on the surface interact more strongly with the surface than those present at the higher loading, and that the former are present at Ti^{3+} surface defect sites, where they are more highly deprotonated than the clusters on other sites. The stronger bonding of the rhenium carbonyls located at the Ti^{3+} defect sites is consistent with the greater electron density available for bonding to the carbonyl ligands in the deprotonated clusters.

We propose a connection between the deprotonation of the rhenium carbonyls and the process of healing of the titania defect (Ti^{3+}) sites to which they are bound, as shown in Scheme 11.2. Adsorption of $H_3Re_3(CO)_{12}$ on TiO_{2vac}, which had a relatively high density of surface defect sites, led to the following: (a) a decrease in the number of Ti^{3+}–OH groups; (b) a decrease in the number of Ti^{3+} sites; (c) a decrease in the number of O^- radical species; and (d) an increase in the number of bridging OH groups.

These observations, occurring during the process of adsorption and deprotonation of $H_3Re_3(CO)_{12}$, are all explained by the representation shown in Scheme 11.2 (we do not rule out other possibilities).

We hypothesize that the changes take place at the oxygen vacancy sites located between Ti^{3+} sites incorporating OH groups and neighboring Ti^{4+} sites incorporating O^- radical species. When $H_3Re_3(CO)_{12}$ is adsorbed at the Ti^{3+} site and donates a proton to it, the proton interacts with the Ti^{4+}–O^- species, resulting in the formation of a OH group, which then becomes bonded to the Ti^{3+} site—thereby healing it and forming a bridging OH group as an O^- radical species is removed and the Ti^{3+} is converted to a Ti^{4+} site—thus, the change involves the transformation of a Ti^{3+}–OH to a Ti^{4+}–OH group.

A limitation of this representation is that it accounts only for the reactions on single Ti^{3+} defect sites on titania, and it is known that other types of defect sites can exist, such as pairs of neighboring Ti^{3+} sites without O^- species. Our data do not distinguish such sites from the ones that we have attempted to model.

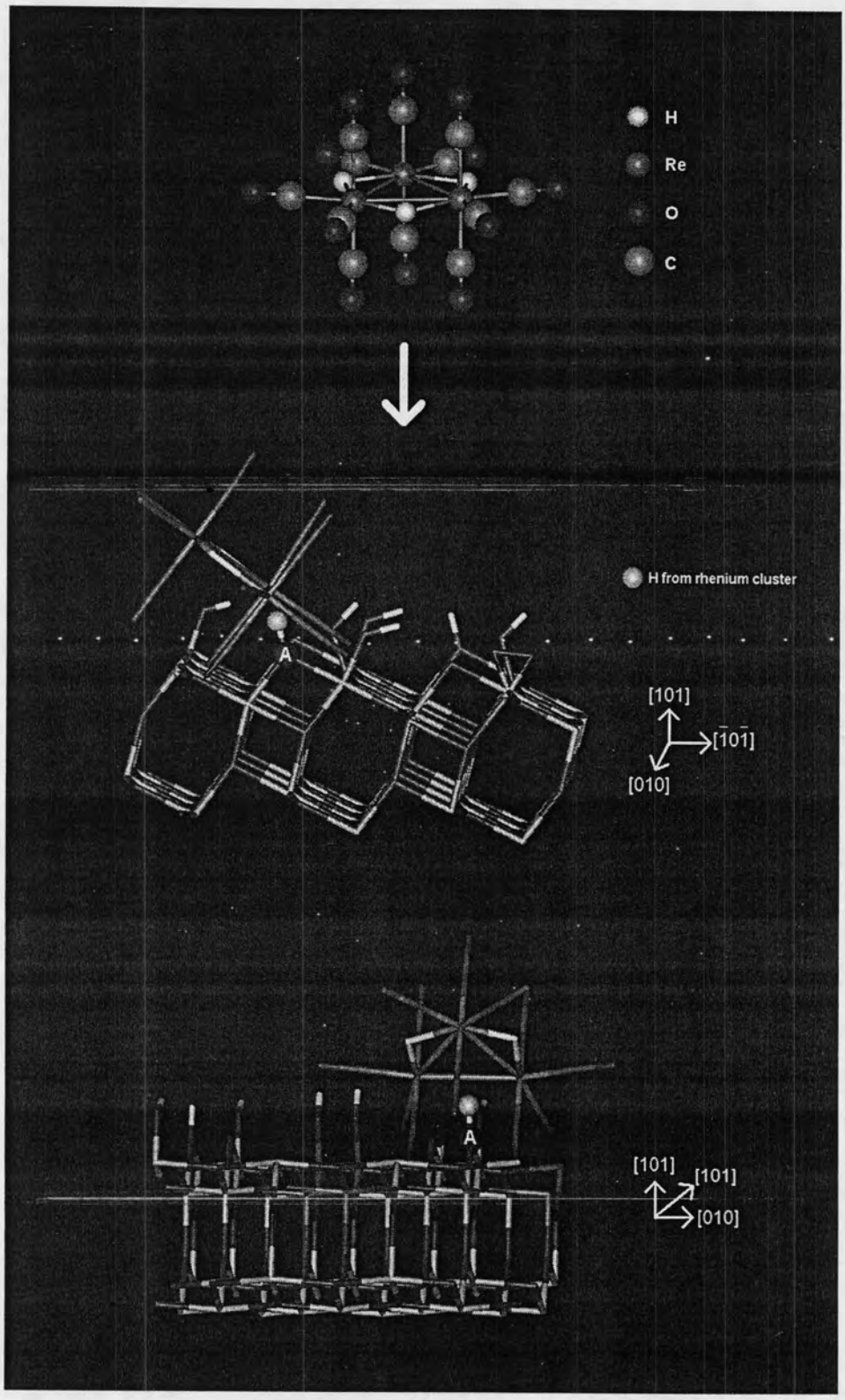

Scheme 11.2: The model representing the surface of anatase before and after rhenium loading